

Development and validation of a subject-specific moving-axis tibiofemoral joint model using MRI and EOS imaging during a quasi-static lunge

Dzialo, C M; Pedersen, P H; Simonsen, C W; Jensen, K K; de Zee, M; Andersen, M S

Published in:
Journal of Biomechanics

DOI (link to publication from Publisher):
[10.1016/j.jbiomech.2018.02.032](https://doi.org/10.1016/j.jbiomech.2018.02.032)

Creative Commons License
CC BY-NC-ND 4.0

Publication date:
2018

Document Version
Accepted author manuscript, peer reviewed version

[Link to publication from Aalborg University](#)

Citation for published version (APA):
Dzialo, C. M., Pedersen, P. H., Simonsen, C. W., Jensen, K. K., de Zee, M., & Andersen, M. S. (2018). Development and validation of a subject-specific moving-axis tibiofemoral joint model using MRI and EOS imaging during a quasi-static lunge. *Journal of Biomechanics*, 72, 71-80.
<https://doi.org/10.1016/j.jbiomech.2018.02.032>

General rights

Copyright and moral rights for the publications made accessible in the public portal are retained by the authors and/or other copyright owners and it is a condition of accessing publications that users recognise and abide by the legal requirements associated with these rights.

- Users may download and print one copy of any publication from the public portal for the purpose of private study or research.
- You may not further distribute the material or use it for any profit-making activity or commercial gain
- You may freely distribute the URL identifying the publication in the public portal -

Take down policy

If you believe that this document breaches copyright please contact us at vbn@aub.aau.dk providing details, and we will remove access to the work immediately and investigate your claim.

Development and validation of a subject-specific moving-axis tibiofemoral joint model using MRI and EOS imaging during a quasi-static lunge

C M Dzialo^{1*}, P H Pedersen², C W Simonsen³, K K Jensen³, M de Zee⁴, M S Andersen¹

¹*Department of Materials and Production, Aalborg University, Fibigerstræde 16, DK-9220 Aalborg, Denmark*

²*Department of Orthopedic Surgery, Aalborg University Hospital, Hobrovej 18-22, DK-9000 Aalborg, Denmark*

³*Department of Radiology, Aalborg University Hospital, Hobrovej 18-22, DK-9000 Aalborg, Denmark*

⁴*Department of Health Science and Technology, Aalborg University, Fredrik Bajers Vej 7D, DK-9220 Aalborg*

Submitted to *Journal of Biomechanics* as an Original Article, 10/2017. Accepted 02/2018.

Keywords: Tibiofemoral joint, secondary joint kinematics, magnetic resonance imaging, musculoskeletal knee model, EOS Imaging

Word count (Introduction through Discussion): 3494

Word count (Introduction through Acknowledgements): 3596

*Corresponding author:

Christine Dzialo

Department of Materials and Production, Aalborg University, Fibigerstræde 16, DK-9220 Aalborg,
Denmark

Tel. +45 42 48 98 90

E-mail: cdz@mp.aau.dk

Abstract

The aims of this study were to introduce and validate a novel computationally-efficient subject-specific tibiofemoral joint model. Subjects performed a quasi-static lunge while micro-dose radiation bi-planar x-rays (EOS Imaging, Paris, France) were captured at roughly 0, 20, 45, 60, and 90 degrees of tibiofemoral flexion. Joint translations and rotations were extracted from this experimental data through 2D-to-3D bone reconstructions, using an iterative closest point optimization technique, and employed during model calibration and validation. Subject-specific moving-axis and hinge models for comparisons were constructed in the AnyBody Modeling System (AMS) from Magnetic Resonance Imaging (MRI)-extracted anatomical surfaces and compared against the experimental data. The tibiofemoral axis of the hinge model was defined between the epicondyles while the moving-axis model was defined based on two tibiofemoral flexion angles (0° and 90°) and the articulation modeled such that the tibiofemoral joint axis moved linearly between these two positions as a function of the tibiofemoral flexion. Outside this range, the joint axis was assumed to remain stationary. Overall, the secondary joint kinematics (ML: medial-lateral, AP: anterior-posterior, SI: superior-inferior, IE: internal-external, AA: adduction-abduction) were better approximated by the moving-axis model with mean differences and standard errors of (ML: $-1.98 \pm 0.37\text{mm}$, AP: $6.50 \pm 0.82\text{mm}$, SI: $0.05 \pm 0.20\text{mm}$, IE: $0.59 \pm 0.36^\circ$, AA: $1.90 \pm 0.79^\circ$) and higher coefficients of determination (R^2) for each clinical measure. While the hinge model achieved mean differences and standard errors of (ML: $-0.84 \pm 0.45\text{mm}$, AP: $10.11 \pm 0.88\text{ mm}$, SI: $0.66 \pm 0.62\text{ mm}$, IE: $-3.17 \pm 0.86^\circ$, AA: $11.60 \pm 1.51^\circ$).

1. Introduction

Musculoskeletal (MS) models are utilized by the scientific community to gain insight on how external forces and movements influence the human body internally, allowing for quantification of muscle, ligament, and joint contact forces without using invasive methods. Studies have shown patients with knee osteoarthritis (KOA) in the tibiofemoral joint tend to have greater adduction angles, and a more medially positioned femur relative to tibia (Farrokhi et al., 2014; Yue et al., 2011; Zeighami et al., 2017; Zeng et al., 2017). Researchers require MS tibiofemoral joint models that capture kinematics properly if the end goal is to investigate pathologies, such as KOA progression, through use of models. Emphasizing the importance of proper model validation.

Existing MS tibiofemoral joint models range from simple to complex depending on their generic qualities and computational time. On one end of the spectrum, researchers idealize the tibiofemoral joint as a hinge joint with a fixed position and orientation (Anderson and Pandy, 2001; Fregly, 2007; Klein Horsman et al., 2007; Marra et al., 2015; Richard et al., 2017). More detailed models include coupling constraints allowing for additional degrees of freedom (DOF) based on tibiofemoral flexion (Delp et al., 1990; Donnelly et al., 2012; Richard et al., 2017; Tsai and Lung, 2014), and sphere-on-plane contact models and parallel spatial mechanisms (Duprey et al., 2010, 2009; Feikes et al., 2003; Gasparutto et al., 2015; Moissenet et al., 2014, 2012; Richard et al., 2017; Wilson et al., 1998). Many of these models are often based on cadaveric geometries and properties, though some models have been given subject-specific properties (Clément et al., 2015; Donnelly et al., 2012; Marra et al., 2015). These simplified generic and subject-specific models allow for computational convenience; but do not capture the elasticity of the joint. At the other end of the spectrum exists computationally complex, 11-12 DOF multibody contact tibiofemoral models (Guess et al., 2014; Hast and Piazza, 2013; Marra et al., 2017, 2015; Smith et al., 2016; Thelen et al., 2014) and finite element models (Adouni et al., 2012; Halonen et al., 2017; Kiapour et al., 2013; Mootanah et al., 2014).

The existing computationally efficient subject-specific tibiofemoral models capture secondary joint kinematics better than their generic counter parts (Clément et al., 2015). Although, sometimes adding subject-specific properties to knee models utilizing parallel mechanisms and/or coupling constraints may prove to be a time-consuming process due to required tuning to avoid singularities (Brito da Luz et al., 2017) and/or full range of motion data (Tsai and Lung, 2014). Our aim is to develop a subject-specific tibiofemoral model that avoids these time-consuming procedures, is computationally efficient, and can display anatomically correct secondary joint kinematics. This paper presents a novel subject-specific tibiofemoral model utilizing a moving-axis based on a linear relationship between two tibiofemoral flexion positions. To validate this approach, we compare the estimates against measured secondary joint kinematics during a quasi-static lunge obtained from EOSTM Imaging biplanar x-rays.

2. Methods

Ten male subjects (age 33 ± 10 years, body mass 79 ± 11 kg, height 1.82 ± 0.07 m, body mass index (BMI) 23.81 ± 2.66 kg/m²) participated in this study. Subjects were categorized as healthy, without pre-existing knee injuries. The following procedures were approved by the Scientific Ethical Committee for the Region of Nordjylland and informed consent was obtained prior to data collection.

2.1 Magnetic Resonance Imaging

Subjects underwent magnetic resonance imaging (MRI) from pelvis to the feet. The 1.5T *OptimaTM MR450w - 70cm* (General Electric Healthcare, Chicago, Illinois, USA) scanner was utilized running a T1W-LAVA-XV-IDEAL, coronal plane scan. To create the lower limb series, subjects were scanned in 3 overlapping sections, moving the table further into the bore, and then stitching the water-only scans together using GE software (Figure 1.A).

2.2 Bi-planar X-ray images

The EOS™ bi-plane x-ray system, shown in the top of Figure 1.B, uses a low-dose biplanar slot-scanning technology; which allows for partial- or full-body imaging collecting a continuous, distortion-free image in two orthogonal planes (Illés and Somoskeöy, 2012; Wybier and Bossard, 2013). We used this system to obtain in-vivo data for model development and validation. Five pairs of orthogonal x-rays images were taken, focusing on the tibiofemoral joint, as the subject performed a quasi-static lunge holding tibiofemoral flexion at roughly 0, 20, 45, 60, and 90 degrees (Figure 1.B bottom). Due to the structural limitations of the EOS scanner, the anterior-posterior (AP) and lateral (LAT) images were taken at approximately 45-degrees to the x-ray tubes (Figure 1.C).

2.3 Segmentation and Registration

The right femur, tibia, and talus bones were manually segmented from the lower limb MRI (Figure 1.A) using Mimics Research 19.0 (Materialise, Belgium). Post-processing was done in Meshmixer (Autodesk, United States of America) and using the contour editing toolbox in Mimics. Stereolithography (STL) surfaces were exported of each bone to obtain subject-specific anatomical landmarks, contact surfaces, and joint centers. In addition, femur and tibia contours were segmented from all biplane x-ray images (Figure 1.C).

To reconstruct femur and tibia positions and orientations for each biplanar x-ray, custom MATLAB (The Mathworks Inc., Natick, MA, USA) code manually transformed the 3D MRI-based bone geometry until its projected contours roughly overlay the bi-plane segmented contours. Hereafter, an iterative closest point optimization method minimized the least-square difference between the bi-planar contours and the 3D geometry generated contour. Subsequently, the positions and orientations were read into AnyBody Modeling System (AMS v 6.1, Aalborg Denmark) to compute the clinical translations and rotations based on ISB standards (Grood and Suntay, 1983). The femur and tibia STL

surfaces obtained from the 0° and 90° EOS reconstructions (Figure 1.D) were used in subject-specific moving-axis tibiofemoral joint development.

2.4 Tibiofemoral coordinate systems kinematic measurement

Identical anatomical coordinate systems (Figure 2) were created for the EOS reconstructions and models following ISB standards (Grood and Suntay, 1983; Wu and Cavanagh, 1995). Anatomical landmarks were defined by averaging clusters of triangles on the STL surfaces at the medial and lateral: femoral epicondyles, tibia edges, and intercondylar tibial eminences. The hip joint center was defined by fitting a sphere to the femoral head surface. The ankle (talocrural) joint axis was defined as a vector joining the centers of two spheres fit to the medial and lateral halves of the talus trochlea, with origin midway between these centers (Parra et al., 2012). The knee translations and rotations were quantified using the anatomical reference frames as described in Grood and Suntay (1983). First, we defined a translation vector directed from the femur origin to the tibia origin. This vector was then projected onto the nonorthogonal unit base vectors, e_1 (femoral fixed body z-axis), e_3 (tibial fixed body y-axis), and e_2 (common perpendicular or floating axis pointing anteriorly) to calculate the medial-lateral, anterior-posterior, and superior-inferior displacements respectively. Relative joint rotations were measured in the sequence of flexion/extension (rotation about femoral fixed axes), abduction/adduction (rotation about the floating axis) and internal/external (rotation about the tibial fixed axis) from the femoral to the tibial anatomical coordinate system.

2.5 Tibiofemoral Model Development

Tibiofemoral models were developed in AMS using the femur and tibia STLs segmented from the lower limb MRI (Figure 3.A *left image*) as rigid body segments.

2.5.1. Data preparation

To establish the moving-axis model, transformation matrices were obtained from the 0° and 90° EOS reconstructions (Figure 3.A *right images*) to the original MRI bone positions for the femur and tibia (Figure 3.B). This was done by using the 3D linear transformation function in AMS, which utilizes a rigid-body least-squares approach based on two sets of landmarks. The tibiofemoral contact areas on the medial and lateral femoral condyles were selected in 3-Matic 11.0 (Materialise, Belgium) for both the 0° and 90° EOS reconstruction bone positions (Figure 3.C). A least-square cylindrical fitting function in MATLAB was used to determine the medial and lateral extension (EFCs) and flexion facet centers (FFCs) (Iwaki et al., 2000), shown in Figure 3.D. These were found by fitting a cylinder, yielding a longitudinal axis and radius, to each of the four contact surfaces. The respective condyle center was defined as the average point along the cylinder axis. The EFCs and the medial FFC were transformed to the femur and tibia segments unaffected; whereas the lateral FFC was separated by a distance equivalent to that between the EFCs, while remaining on the FFC axis.

2.5.2. Conceptual model

The femoral and tibial EFCs and FFCs were used to define a tibiofemoral model with an axis passing through EFCs when the flexion angle corresponds to the 0° EOS reconstruction and through FFCs when the flexion angle corresponds with the 90° EOS reconstruction. In between, the tibiofemoral axis is assumed to move linearly from the EFCs to the FFCs as a function of tibiofemoral flexion. When the tibiofemoral flexion is below the EOS 0° or above the EOS 90° angles, the tibiofemoral axis is assumed to remain fixed through the EFCs and FFCs, respectively.

2.5.3. Kinematic model

To model this conveniently in AMS, two additional rigid segments were introduced, so-called invisible femur and invisible tibia, which were used to move the tibiofemoral flexion axis relative to the femur and tibia according to the relationship above. To describe this mathematically, a full

Cartesian formulation was applied, in which the position and orientation of each body relative to the global coordinates system was used as the unknowns and collectively denoted, \mathbf{q} (Figure 4). The position vector of each body is denoted ${}_{(i)}\mathbf{r} = [{}_{(i)}x \quad {}_{(i)}y \quad {}_{(i)}z]^T$ and the orientation is described by four Euler parameters ${}_{(i)}\mathbf{p} = [{}_{(i)}e_0 \quad {}_{(i)}e_1 \quad {}_{(i)}e_2 \quad {}_{(i)}e_3]^T$, where the left sub-script denotes the i th segment, i.e. $i = \{T, F, IT, IF\}$ with T for tibia, F for femur, IT for invisible tibia and IF for invisible femur. To formulate the equations, the rotation matrix of each body is required and denoted ${}_{(i)}\mathbf{A} = [{}_{(i)}\mathbf{a}_x \quad {}_{(i)}\mathbf{a}_y \quad {}_{(i)}\mathbf{a}_z]$, where ${}_{(i)}\mathbf{a}_x$, ${}_{(i)}\mathbf{a}_y$ and ${}_{(i)}\mathbf{a}_z$ are the first, second and third columns, respectively. Although the rotation matrix is a function of Euler parameters, the function argument is omitted to keep the equations concise. For each segment, coordinates systems are defined and the required points for the tibiofemoral model are transformed into these coordinate systems. For the invisible tibia and invisible femur, medial and lateral points were defined along the z-axis separated by a distance equivalent to that between the EFCs. The orientation of the y- and x-axis are irrelevant for axis movement but defined with the y-axis of each invisible segment orthogonal to the z-axis (pointing towards the hip center and away from the ankle joint center respectively), and the x-axis orthogonal to the y- and z- axis. The points on all the segments are systematically named ${}_{(i)}\mathbf{s}'_j$ where j is denoting the point name, e.g. ${}_{(T)}\mathbf{s}'_{\text{LFFC}}$ is the position vector of the lateral FFC in the tibial coordinate system. With this, the holonomic constraint equations to describe the tibiofemoral model can be expressed as:

$$\Phi(\mathbf{q}) = \begin{bmatrix} {}^{(F)}\mathbf{f}_{MP} - {}^{(IF)}\mathbf{r} - {}^{(IF)}\mathbf{A} {}^{(IF)}\mathbf{s}'_{MP} \\ {}^{(T)}\mathbf{f}_{MP} - {}^{(IT)}\mathbf{r} - {}^{(IT)}\mathbf{A} {}^{(IT)}\mathbf{s}'_{MP} \\ \left({}^{(IF)}\mathbf{A}^T \left({}^{(F)}\mathbf{f}_{LP} - {}^{(IF)}\mathbf{r} - {}^{(IF)}\mathbf{A} {}^{(IF)}\mathbf{s}'_{LP} \right) \right)_{xy} \\ \left({}^{(IT)}\mathbf{A}^T \left({}^{(T)}\mathbf{f}_{LP} - {}^{(IT)}\mathbf{r} - {}^{(IT)}\mathbf{A} {}^{(IT)}\mathbf{s}'_{LP} \right) \right)_{xy} \\ {}^{(IF)}\theta_z \\ {}^{(IT)}\theta_z \\ {}^{(IF)}\mathbf{r} - {}^{(IT)}\mathbf{r} \\ {}^{(IF)}\mathbf{a}_z^T {}^{(IT)}\mathbf{a}_y \\ {}^{(IF)}\mathbf{a}_z^T {}^{(IT)}\mathbf{a}_x \\ {}^{(F)}\mathbf{p}^T {}^{(F)}\mathbf{p} - 1 \\ {}^{(IF)}\mathbf{p}^T {}^{(IF)}\mathbf{p} - 1 \\ {}^{(T)}\mathbf{p}^T {}^{(T)}\mathbf{p} - 1 \\ {}^{(IT)}\mathbf{p}^T {}^{(IT)}\mathbf{p} - 1 \end{bmatrix} = \mathbf{0} \quad (1)$$

where

$${}^{(F)}\mathbf{f}_{MP} = \begin{cases} {}^{(T)}\mathbf{r}_{MEFC} & \theta_{TF} < \theta_{EOS}^0 \\ {}^{(T)}\mathbf{r}_{MEFC} (1-\nu) + {}^{(T)}\mathbf{r}_{MFFC} \nu & \theta_{EOS}^0 \leq \theta_{TF} \leq \theta_{EOS}^{90} \\ {}^{(T)}\mathbf{r}_{MFFC} & \theta_{EOS}^{90} < \theta_{TF} \end{cases} \quad (2)$$

and

$$\nu = \frac{\theta_{TF} - \theta_{EOS}^0}{\theta_{EOS}^{90} - \theta_{EOS}^0} \quad (3)$$

${}^{(F)}\mathbf{f}_{LP}$, ${}^{(T)}\mathbf{f}_{MP}$ and ${}^{(T)}\mathbf{f}_{LP}$ are defined in the same manner using instead the lateral points of femur, and the medial and lateral points of tibia respectively. θ_{TF} is the tibiofemoral flexion angle measured between the femur and tibia anatomical coordinate systems; θ_{EOS}^0 and θ_{EOS}^{90} are the tibiofemoral flexion angles corresponding to the EOS 0° and EOS 90° scans. ${}^{(IF)}\theta_z$ and ${}^{(IT)}\theta_z$ are Euler angles around the z-axis of the invisible femur and invisible tibia relative to the femur and tibia anatomical frames respectively, measured with a rotation sequence of z-x-y. The top two equations in Equation

(1) constrain the medial point of the invisible segments to a position in between the EFC and FFC depending on the tibiofemoral flexion. Similarly, the third and fourth equations constrain the x and y coordinates of the lateral point of each invisible segment to a position between the EFC and FFC. The fifth and sixth equation ensure zero rotation about the z-axis relative to the anatomical frames for the invisible segments. Equations seven to nine enforce a revolute joint between the invisible segments by constraining their origins to be at the same position in the global coordinate system and ensuring only relative rotation around the z-axis is allowed. The last four equations ensure the Euler parameters have unity length.

Equation (1) provides 21 constraint equations, however the total system has 28 coordinates, i.e. seven for each rigid body. Therefore, seven equations are still required to perform a kinematically determinate analysis. These are specified as:

$$\Phi^{(d)}(\mathbf{q}, t) = \begin{bmatrix} {}^{(T)}\mathbf{r} \\ {}^{(T)}\theta_x \\ {}^{(T)}\theta_y \\ {}^{(T)}\theta_z \\ \theta_{TF} - at - b \end{bmatrix} = \mathbf{0} \quad (4)$$

where ${}^{(T)}\theta_x$, ${}^{(T)}\theta_y$ and ${}^{(T)}\theta_z$ are the Euler angles of tibia relative to the global coordinate system measured in the sequence z-x-y. These equations enforce tibia to align with the global coordinate system and control the tibiofemoral flexion angle, θ_{TF} , to flex with a constant velocity, a , and with a flexion angle of b at time $t = 0$. b was specified as the tibiofemoral flexion angle captured in EOS 0° and, as the knee kinematics is independent of flexion velocity, a was set to 110°s^{-1} . The constraint equations in (1) and (4) were simultaneously solved in AMS using a Newton-Raphson-based nonlinear equation solver with time intervals set to ensure that knee flexion angles both before and after the EOS 0° and EOS 90° were included.

2.5.4 Comparison model

In addition, a subject-specific hinge model was created for each subject to investigate how well the moving-axis model performs against a commonly used tibiofemoral joint in the musculoskeletal community. The hinge joint was defined by a line passing through the medial and lateral femoral epicondyles (Churchill et al., 1998) and driven from 0° to 110° flexion.

2.6 Model Evaluation and Statistics

Tibiofemoral kinematics were extracted from EOS scans at five conditions of varying tibiofemoral flexion. Model predicted results were extracted at these five corresponding conditions per subject (n=10). Since the 0° and 90° EOS reconstructions were used for the moving-axis model calibrations, these did not provide any model prediction capabilities and were excluded when evaluating the moving-axis model. The model (hinge and moving-axis) predictions were evaluated against EOS experimental measurements and each other, in terms of mean difference and coefficient of determination (R^2). Fifteen one-way repeated measures ANOVAs (5 clinical measures at 3 lunge conditions) were performed with post-hoc tests using Bonferroni adjustments ($\alpha=0.01$) for multiple comparisons. The data was tested for normality using a Shapiro-Wilk tests and adjusted for small sample size using the Greenhouse-Geisser estimates of sphericity (Maxwell et al., 2013).

3. Results

The tibiofemoral secondary joint kinematics of each subject (n=10) were extracted (Figure 5) from the EOS reconstructions (circles), hinge (left), and moving-axis (right) models. More subject deviation existed in rotational measures compared to translational. The experimental abduction and internal rotations increased with tibiofemoral flexion (0° to 90°); the moving-axis models agreed, while the hinge models opposed with this trend. The superior/inferior (SI) displacement of the hinge model remained constant during the entire flexion/extension (FE) cycle contrasting the in vivo

experimental (EOS) results which decreased. The moving-axis models responded similarly to the EOS data. The EOS data showed clear anterior/posterior (AP) displacements, which is captured by the moving-axis model but not by the hinge.

The mean kinematic parameters for each quasi-static lunge condition were calculated for experimental EOS data (Table 1), moving-axis model output (Table 2), and hinge model output (Table 3). In addition, minimum, maximum, and range of motion values (mean \pm standard deviation) were extracted (Table 1-3). Overall, the moving-axis model better captured the EOS ROM which was often underestimated by the hinge model.

Mean differences (MD) and standard error (SE) between models and experimental data were recorded (Table 4) and R^2 values are presented (Table 5) to compare model predictive capabilities. Almost exclusively, the moving-axis model showed lower mean differences and higher R^2 values when compared to the hinge. However, at lower angles of flexion (20° and 45°) the moving-axis ML displacements are significantly different (MD \pm SE: -2.43 ± 0.35 mm and -2.31 ± 0.44 mm) than the experimental data ($p\text{-value} \leq 0.01$). In addition, moving-axis and hinge models significantly underestimated experimental AP displacements (average MD \pm SE: 6.50 ± 0.82 mm and 10.11 ± 0.88 mm respectively) for all lunge angles. The hinge model varied significantly from the experimental data in abduction/adduction (AA) and internal/external (IE) rotations (average MD \pm SE: $-3.17 \pm 0.86^\circ$ and $11.60 \pm 1.51^\circ$). While no significant differences were found between the moving-axis model and experimental data with respect to rotational measures (see Supplementary Table for p-values and confidence intervals).

When comparing the models themselves, significant differences were more prevalent in rotational measures than translations. The AP displacement significantly differs in the hinge joint model (MD \pm SE: $7.40 \pm 1.59^\circ$) compared to the moving-axis model in deeper tibiofemoral flexion (60°). While

the AA and IE rotations significantly differ in the hinge model (average MD \pm SE: $-3.76 \pm 0.82^\circ$ and $9.70 \pm 1.10^\circ$) when compared to the moving-axis model for all lunge conditions except AA rotation at 20° tibiofemoral flexion.

4. Discussion

In this study, we introduced a novel moving-axis tibiofemoral model and validated it against experimental EOS data. An ongoing cadaver validation study, currently unpublished, has found an accuracy of $0.39 \pm 0.48^\circ$ for rotations and 0.72 ± 0.88 mm for translations using the same EOS reconstruction method utilized in this study. Our results showed that the moving-axis tibiofemoral model better represents the EOS secondary kinematics during a quasi-static lunge as compared to a hinge model. The moving-axis seems to slightly overestimate medial-lateral displacement and underestimate anterior-posterior displacement, while the hinge underestimates all joint displacements and rotations due to its stationary axis. To ensure the EOS data reasonably represented healthy tibiofemoral kinematics we compared it to studies examining similar knee flexion movements (Dennis et al., 2005; Moro-oka et al., 2008; Qi et al., 2013; Varadarajan et al., 2009).

We found translational ROMs of 3.25 ± 1.48 mm (ML) and 14.09 ± 5.09 mm (AP) during $3.48 \pm 5.62^\circ$ to $86.59 \pm 8.54^\circ$ TF flexion; which are similar to ML (2.5 ± 2.5 mm & 1.5 ± 2 mm) and AP (11.5 ± 4 mm & 16.5 ± 4 mm) displacements extracted from 0 - 90° TF flexion in bi-planar fluoroscopy lunge studies (Qi et al., 2013; Varadarajan et al., 2009), respectively. In addition, single plane fluoroscopy studies, capturing a similar knee flexion movement (Dennis et al., 2005; Moro-oka et al., 2008), have displayed AP displacements of (10-11mm) during 0 - 90° TF flexion, agreeing with our findings. We recorded rotational ROMs of $3.92 \pm 2.11^\circ$ (AA) and $11.84 \pm 5.23^\circ$ (IE) supporting the bi-planar studies (Qi et al., 2013; Varadarajan et al., 2009) which display AA ($2.75 \pm 1.5^\circ$ & $1.5 \pm 3^\circ$) and IE ($6 \pm 6^\circ$ & $10 \pm 5^\circ$), respectively; while the single plane fluoroscopy studies, we

investigated, showed slightly higher IE rotations ranging from 15° to $21 \pm 3^{\circ}$ (Dennis et al., 2005; Moro-oka et al., 2008).

Why does the research community need another simple subject-specific tibiofemoral model? It has been shown, when using multibody kinematics optimization (Begon et al., 2018; Lu and O'Connor, 1999) secondary joint kinematics can be improved by employing more advanced (compared to hinge) and subject-specific tibiofemoral models (Clément et al., 2015). The moving-axis model can be used to reconstruct movements measured in a gait lab by simply replacing the constant velocity TF flexion driver with soft constraints between model markers and measured skin markers (Andersen et al., 2009). Furthermore, the moving-axis tibiofemoral model is simply calibrated from two poses; which avoids obtaining full range of motion data, sometimes required in models using coupling constraints. Moreover, no additional tuning is required to run the moving-axis model, which is often needed to avoid singularities in parallel mechanism or sphere-on-plane models (Brito da Luz et al., 2017; Habachi et al., 2015). Additionally, the moving-axis model can easily be extended to the patellofemoral joint.

The moving-axis tibiofemoral model has its limitations. Specifically, the kinematics will remain the same independent of external load, which for some applications may play a role. Complex multibody contact models (Guess et al., 2014; Marra et al., 2017, 2015; Smith et al., 2017; Thelen et al., 2014) were established to avoid these limitations; these models are much more computationally expensive and therefore applied on smaller cohorts. Although large improvements were achieved by modeling the TF joint as a moving-axis, creating a linear relationship between EFC and FFC axes may not capture the entire trend. The moving-axis model is calibrated off two poses (0° and 90°). Conceivably, an infinite number of poses could be used to calibrate this model; however, this will increase the radiation exposure and eliminate the EOS means of validation. Additionally, a positioning jig to keep quasi-static flexion angles consistent amongst subjects was not used. Although not a primary aim, it

may have been beneficial to ensure lunge consistency to more effectively compare secondary joint kinematics between subjects. Furthermore, the images were captured quasi-statically for one movement type, so the results cannot be generalized to other activities.

In conclusion, we have developed a new approach in constructing the tibiofemoral joint in musculoskeletal modeling. This method allows for a computational fast model with subject-specific geometries and kinematics. The results indicate a piecewise linear model constructed from two active tibiofemoral positions, acquired from EOS imaging technology, can accurately represent secondary kinematics. Furthermore, a moving-axis joint can better predict most experimentally observed tibiofemoral joint rotations and translations when compared to the commonly used hinge joint.

Conflict of Interest

Mark de Zee is co-founder of the company AnyBody Technology A/S, owning the AnyBody Modeling System, which was used for the simulations. Mark de Zee is a minority shareholder on the company.

Acknowledgements

This study was performed under the KNEEMO Initial Training Network, funded by the European Union's Seventh Framework Programme for research, technological development, and demonstration under Grant Agreement No. 607510 (www.kneemo.eu). This work was also supported by the Sapere Aude program of the Danish Council for Independent Research under grant no. DFF-4184-00018 to M. S. Andersen and the Innovation Fund Denmark under the Individualized Osteoarthritis Intervention project.

References

Adouni, M., Shirazi-Adl, A., Shirazi, R., 2012. Computational biodynamics of human knee joint in

- gait: From muscle forces to cartilage stresses. *J. Biomech.* 45, 2149–2156.
<https://doi.org/10.1016/j.jbiomech.2012.05.040>
- Andersen, M.S., Damsgaard, M., Rasmussen, J., 2009. Kinematic analysis of over-determinate biomechanical systems. *Comput. Methods Biomech. Biomed. Engin.* 12, 371–384.
<https://doi.org/10.1080/10255840802459412>
- Anderson, F.C., Pandy, M.G., 2001. Dynamic optimization of human walking. *J. Biomech. Eng.* 123, 381–390. <https://doi.org/10.1115/1.1392310>
- Begon, M., Andersen, M.S., Dumas, R., 2018. Multibody kinematic optimization for the estimation of upper and lower limb human joint kinematics: a systematic review. *J. Biomech. Eng.* 140, 1–11. <https://doi.org/10.1115/1.4038741>
- Brito da Luz, S., Modenese, L., Sancisi, N., Mills, P.M., Kennedy, B., Beck, B.R., Lloyd, D.G., 2017. Feasibility of using MRIs to create subject-specific parallel-mechanism joint models. *J. Biomech.* 53, 45–55. <https://doi.org/10.1016/j.jbiomech.2016.12.018>
- Churchill, D.L., Incavo, S.J., Johnson, C.C., Beynnon, B.D., 1998. The transepicondylar axis approximates the optimal flexion axis of the knee. *Clin. Orthop. Relat. Res.* 111–118.
- Clément, J., Dumas, R., Hagemester, N., de Guise, J.A., 2015. Soft tissue artifact compensation in knee kinematics by multi-body optimization: Performance of subject-specific knee joint models. *J. Biomech.* 48, 3796–3802. <https://doi.org/10.1016/j.jbiomech.2015.09.040>
- Delp, S.L., Loan, J.P., Hoy, M.G., Zajac, F.E., Topp, E.L., Rosen, J.M., 1990. An Interactive Graphics-Based Model of the Lower Extremity to Study Orthopaedic Surgical Procedures 37, 757–767.

Dennis, D.A., Mahfouz, M.R., Komistek, R.D., Hoff, W., 2005. In vivo determination of normal and anterior cruciate ligament-deficient knee kinematics 38, 241–253.

<https://doi.org/10.1016/j.jbiomech.2004.02.042>

Donnelly, C.J., Lloyd, D.G., Elliott, B.C., Reinbolt, J.A., 2012. Optimizing whole-body kinematics to minimize valgus knee loading during sidestepping : Implications for ACL injury risk. J.

Biomech. 45, 1491–1497. <https://doi.org/10.1016/j.jbiomech.2012.02.010>

Duprey, S., Cheze, L., Dumas, R., 2010. Influence of joint constraints on lower limb kinematics estimation from skin markers using global optimization. J. Biomech. 43, 2858–2862.

<https://doi.org/10.1016/j.jbiomech.2010.06.010>

Duprey, S., Chèze, L., Dumas, R., 2009. A constraint-based approach to model the lower limb:

preliminary results for running motions. Comput. Methods Biomech. Biomed. Engin. 12, 105–106. <https://doi.org/10.1080/10255840903077352>

Farrokhi, S., Voycheck, C.A., Klatt, B.A., Gustafson, J.A., Tashman, S., Fitzgerald, G.K., 2014.

Altered tibiofemoral joint contact mechanics and kinematics in patients with knee osteoarthritis and episodic complaints of joint instability. Clin. Biomech. 29, 629–635.

<https://doi.org/10.1016/j.clinbiomech.2014.04.014>

Feikes, J.D., Connor, J.J., Zavatsky, A.B., 2003. A constraint-based approach to modelling the

mobility of the human knee joint. J. Biomech. 36, 125–129. [https://doi.org/10.1016/S0021-9290\(02\)00276-2](https://doi.org/10.1016/S0021-9290(02)00276-2)

Fregly, B.J., 2007. Design of Patient-Specific Gait Modifications for Knee Osteoarthritis

Rehabilitation. IEEE Trans. Med. Imaging 29, 997–1003.

<https://doi.org/10.1016/j.biotechadv.2011.08.021>.Secreted

- Gasparutto, X., Sancisi, N., Jacquelin, E., Parenti-Castelli, V., Dumas, R., 2015. Validation of a multi-body optimization with knee kinematic models including ligament constraints. *J. Biomech.* 48, 1141–1146. <https://doi.org/10.1016/j.jbiomech.2015.01.010>
- Grood, E.S., Suntay, W., 1983. A Joint Coordinate System for the Clinical Description of Three-Dimensional Motions: Application to the Knee. *J. Biomech. Engineering* 105, 136–144.
- Guess, T.M., Stylianou, A.P., Kia, M., 2014. Concurrent prediction of muscle and tibiofemoral contact forces during treadmill gait. *J. Biomech. Eng.* 136, 021032:1-9. <https://doi.org/10.1115/1.4026359>
- Habachi, A. El, Moissenet, F., Duprey, S., Cheze, L., Dumas, R., 2015. Global sensitivity analysis of the joint kinematics during gait to the parameters of a lower limb multi - body model. *Med. Biol. Eng. Comput.* 655–667. <https://doi.org/10.1007/s11517-015-1269-8>
- Halonen, K.S., Dzialo, C.M., Mannisi, M., Venäläinen, M.S., Zee, M. De, Andersen, M.S., 2017. Workflow assessing the effect of gait alterations on stresses in the medial tibial cartilage – combined musculoskeletal modelling and finite element analysis. *Sci. Rep.* 7, 17396. <https://doi.org/10.1038/s41598-017-17228-x>
- Hast, M.W., Piazza, S.J., 2013. Dual-joint modeling for estimation of total knee replacement contact forces during locomotion. *J. Biomech. Eng.* 135, 21013. <https://doi.org/10.1115/1.4023320>
- Illés, T., Somoskeöy, S., 2012. The EOS™ imaging system and its uses in daily orthopaedic practice. *Int. Orthop.* <https://doi.org/10.1007/s00264-012-1512-y>
- Iwaki, H., Pinskerova, V., Freeman, M.A.R., 2000. Tibiofemoral movement 1: the shapes and relative movements of the femur and tibia in the unloaded cadaver knee. *J. Bone Joint Surg.*

Br. 82, 1189–1195. <https://doi.org/10.1302/0301-620x.82b8.10717>

Kiapour, A., Kiapour, A.M., Kaul, V., Quatman, C.E., Wordeman, S.C., Hewett, T.E.,
Demetropoulos, C.K., Goel, V.K., 2013. Finite Element Model of the Knee for Investigation of
Injury Mechanisms: Development and Validation. *J. Biomech. Eng.* 136, 11002.
<https://doi.org/10.1115/1.4025692>

Klein Horsman, M.D., Koopman, H.F.J.M., van der Helm, F.C.T., Prosé, L.P., Veeger, H.E.J.,
2007. Morphological muscle and joint parameters for musculoskeletal modelling of the lower
extremity. *Clin. Biomech.* 22, 239–247. <https://doi.org/10.1016/j.clinbiomech.2006.10.003>

Lu, T.W., O'Connor, J.J., 1999. Bone position estimation from skin marker co-ordinates using
global optimisation with joint constraints. *J. Biomech.* 32, 129–134.
[https://doi.org/10.1016/S0021-9290\(98\)00158-4](https://doi.org/10.1016/S0021-9290(98)00158-4)

Marra, M.A., Strzelczak, M., Heesterbeek, P.J.C., van de Groes, S.A.W., Janssen, D.W., Koopman,
B.F.J.M., Wymenga, A.B., Verdonschot, N.J.J., 2017. Anterior referencing of tibial slope in
total knee arthroplasty considerably influences knee kinematics: a musculoskeletal simulation
study. *Knee Surgery, Sport. Traumatol. Arthrosc.* 1–9. <https://doi.org/10.1007/s00167-017-4561-3>

Marra, M.A., Vanheule, V., Fluit, R., Koopman, B.H.F.J.M., Rasmussen, J., Verdonschot, N.,
Andersen, M.S., 2015. A Subject-Specific Musculoskeletal Modeling Framework to Predict In
Vivo Mechanics of Total Knee Arthroplasty. *J. Biomech. Eng.* 137, 20904.
<https://doi.org/10.1115/1.4029258>

Maxwell, S.E., Delaney, H.D., Planer, J., 2013. Stats: Designing Experiments Ch9-10. *J. Chem. Inf.*
Model. 53, 1689–1699. <https://doi.org/10.1017/CBO9781107415324.004>

- Moissenet, F., Chèze, L., Dumas, R., 2014. A 3D lower limb musculoskeletal model for simultaneous estimation of musculo-tendon, joint contact, ligament and bone forces during gait. *J. Biomech.* 47, 50–58. <https://doi.org/10.1016/j.jbiomech.2013.10.015>
- Moissenet, F., Chèze, L., Dumas, R., 2012. Anatomical kinematic constraints: Consequences on musculo-tendon forces and joint reactions. *Multibody Syst. Dyn.* 28, 125–141. <https://doi.org/10.1007/s11044-011-9286-3>
- Mootanah, R., Imhauser, C.W., Reisse, F., Carpanen, D., Walker, R.W., Koff, M.F., Lenhoff, M.W., Rozbruch, R., Fragomen, A.T., Kirane, Y.M., Rozbruch, S.R., Dewan, Z., Cheah, K., Dowell, J.K., Hillstrom, H.J., 2014. Development and Verification of a Computational Model of the Knee Joint for the Evaluation of Surgical Treatments for Osteoarthritis. *Comput. Methods Biomech. Biomed. Engin.* <https://doi.org/10.1080/10255842.2014.899588>
- Moro-oka, T.-A., Hamai, S., Miura, H., Shimoto, T., Higaki, H., Fregly, B.J., Iwamoto, Y., Banks, S.A., 2008. Dynamic Activity Dependence of In Vivo Normal Knee Kinematics. *J. Orthop. Res.* 26, 428–434. <https://doi.org/10.1002/jor.20488>
- Parra, W.C.H., Chatterjee, H.J., Soligo, C., 2012. Calculating the axes of rotation for the subtalar and talocrural joints using 3D bone reconstructions. *J. Biomech.* 45, 1103–1107. <https://doi.org/10.1016/j.jbiomech.2012.01.011>
- Qi, W., Hosseini, A., Tsai, T.Y., Li, J.S., Rubash, H.E., Li, G., 2013. In vivo kinematics of the knee during weight bearing high flexion. *J. Biomech.* 46, 1576–1582. <https://doi.org/10.1016/j.jbiomech.2013.03.014>
- Richard, V., Cappozzo, A., Dumas, R., 2017. Comparative assessment of knee joint models used in multi-body kinematics optimisation for soft tissue artefact compensation. *J. Biomech.* 62, 95–

101. <https://doi.org/10.1016/j.jbiomech.2017.01.030>
- Smith, C.R., Lenhart, B.S.R.L., Thelen, D.G., Kaiser, J., Vignos, M.F., 2016. Influence of Ligament Properties on Tibiofemoral Mechanics in Walking. *J. Knee Surgery* 29, 99–106.
- Smith, C.R., Vignos, M.F., Lenhart, R.L., Kaiser, J., 2017. The Influence of Component Alignment and Ligament Properties on Tibiofemoral Contact Forces in Total Knee Replacement. *J. Biomech. Eng.* 138, 021017:1-10. <https://doi.org/10.1115/1.4032464>
- Thelen, D.G., Won Choi, K., Schmitz, A.M., 2014. Co-simulation of neuromuscular dynamics and knee mechanics during human walking. *J. Biomech. Eng.* 136, 21033. <https://doi.org/10.1115/1.4026358>
- Tsai, M.-J., Lung, H.-Y., 2014. Two-phase optimized inverse kinematics for motion replication of real human models. *J. Chinese Inst. Eng.* 37, 899–914. <https://doi.org/10.1080/02533839.2014.904474>
- Varadarajan, K.M., Gill, T.J., Freiberg, A.A., Rubash, H.E., Li, G., 2009. Gender differences in trochlear groove orientation and rotational kinematics of human knees. *J. Orthop. Res.* 27, 871–878. <https://doi.org/10.1002/jor.20844>
- Wilson, D.R., Feikes, J.D., Connor, J.J., 1998. Ligaments and articular contact guide passive knee flexion. *J. Biomech.* 31, 1127–1136. [https://doi.org/10.1016/S0021-9290\(98\)00119-5](https://doi.org/10.1016/S0021-9290(98)00119-5)
- Wu, G., Cavanagh, P.R., 1995. ISB Recommendations in the Reporting for Standardization of Kinematic Data. *J. Biomech.* 28, 1257–1261. [https://doi.org/10.1016/0021-9290\(95\)00017-C](https://doi.org/10.1016/0021-9290(95)00017-C)
- Wybier, M., Bossard, P., 2013. Musculoskeletal imaging in progress: The EOS imaging system. *Jt.*

Bone Spine. <https://doi.org/10.1016/j.jbspin.2012.09.018>

Yue, B., Varadarajan, K.M., Moynihan, A.L., Liu, F., Rubash, H.E., Li, G., 2011. Kinematics of medial osteoarthritic knees before and after posterior cruciate ligament retaining total knee arthroplasty. *J. Orthop. Res.* 29, 40–46. <https://doi.org/10.1002/jor.21203>

Zeighami, A., Dumas, R., Kanhonou, M., Hagemeister, N., Lavoie, F., de Guise, J.A., Aissaoui, R., 2017. Tibio-femoral joint contact in healthy and osteoarthritic knees during quasi-static squat: A bi-planar X-ray analysis. *J. Biomech.* 53, 178–184.

Zeng, X., Ma, L., Lin, Z., Huang, W., Huang, Z., Zhang, Y., Mao, C., 2017. Relationship between Kellgren-Lawrence score and 3D kinematic gait analysis of patients with medial knee osteoarthritis using a new gait system. *Sci. Rep.* 7, 4080. <https://doi.org/10.1038/s41598-017-04390-5>

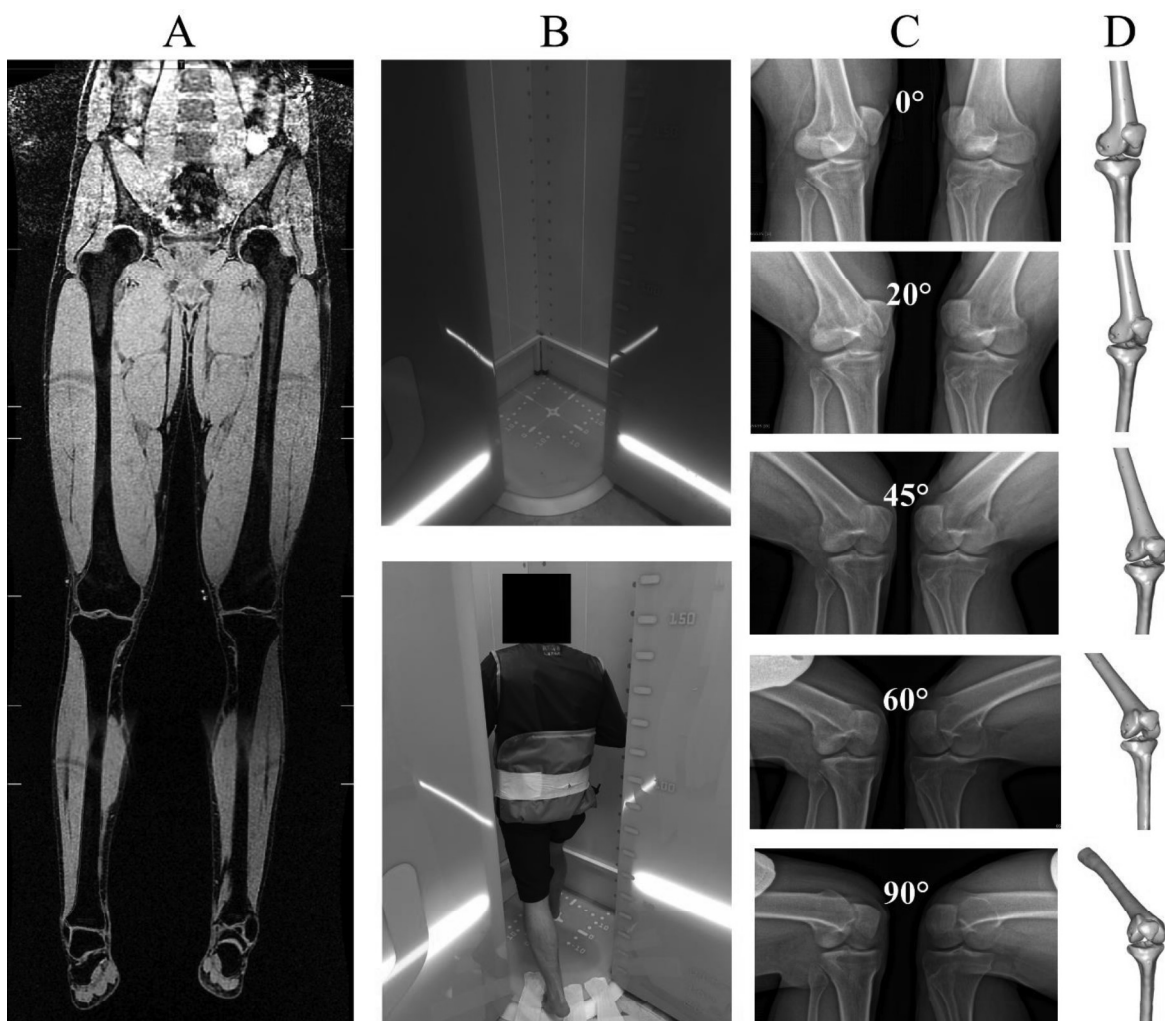


FIGURE 1—A method of combining MR and EOS Imaging technology: A, Development of 3D knee geometry using a stack of coronal MR images; B, and acquisition of quasi-static lunge (lower image) using two orthogonally positioned low dose x-rays (top image). C, Bi-planar EOS images were taken at roughly 0° , 20° , 45° , 60° , and 90° tibiofemoral flexion. D, Bone positions were determined by combining the 3D knee model with the bi-planar contours and applying optimization methods.

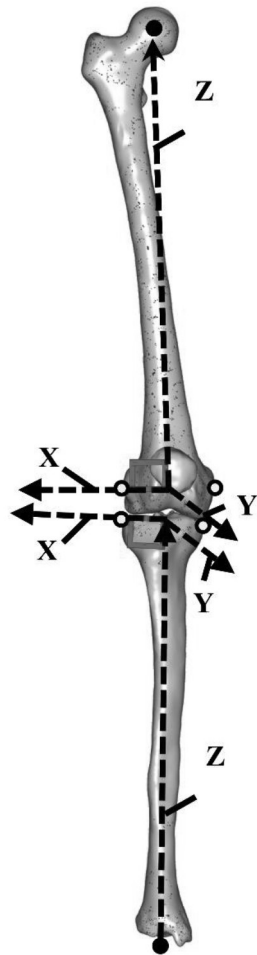


FIGURE 2—Right leg anatomical axes definitions. Femur: Z-axis (longitudinal axis) was defined from hip joint center to midpoint between medial and lateral epicondyles. X-axis (medial-lateral axis) was defined to be orthogonal to the Z-axis axis and pointing towards the medial epicondyle. Y-axis was orthogonal to both the Z and X axes and pointing anteriorly. Tibia: Z-axis was defined from the talocrural joint center (Parra et al. 2012) to the midpoint between the medial tibia edge and lateral tibia edge. X-axis (medial-lateral axis) was defined to be orthogonal to the Z-axis and pointing towards the medial tibia edge. Y-axis was orthogonal to both the Z and X axes and pointing anteriorly.

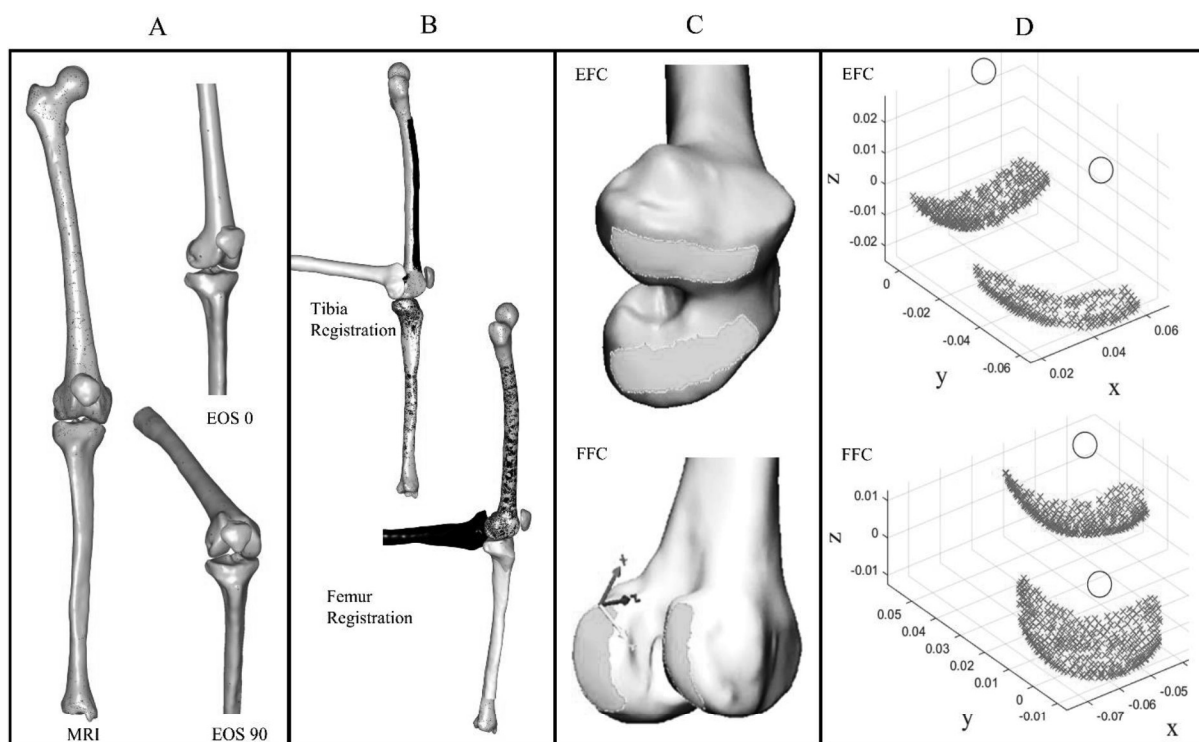


FIGURE 3—Overview of extension (EFC) and flexion facet centers (FFC) axes definition: A, Lower limb MRI segmentation and resulting bone positions from EOS 0 and 90 reconstructions to obtain respective transformation matrices. B, Femur and Tibia Registrations of the EOS 0 and 90 STLs on to MRI STLs. C, Tibiofemoral contact surface selection on EOS 0 and EOS 90 Femur STLs. D, Cylinder fits on medial and lateral femoral condyle surface selections with resulting EFCs and FFCs.

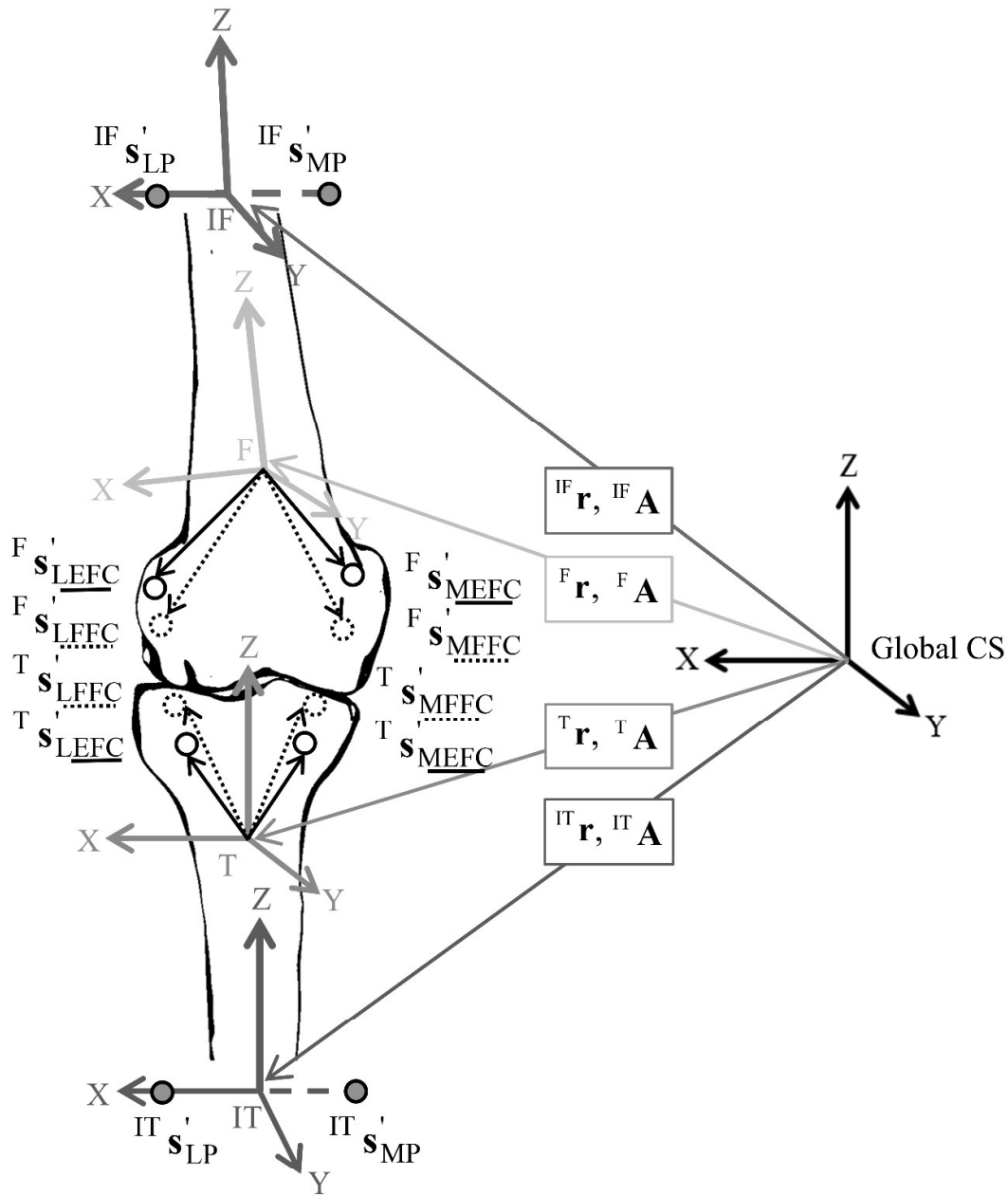


FIGURE 4—Schematic of position vectors and rotation matrices of the femur, tibia, invisible femur, and invisible tibia rigid body segments with respect to the global coordinate system. The black coordinate system refers to the global, yellow: femur, red: invisible femur, green: tibia, and blue: invisible tibia. Solid colored arrows represent position vector and rotation matrices between global coordinate systems and respective rigid body segment coordinate systems. Solid black lines represent position vectors of EFC points in femoral/tibial coordinate systems while dotted lines depict position vectors of FFC points in femoral/tibia coordinate systems.

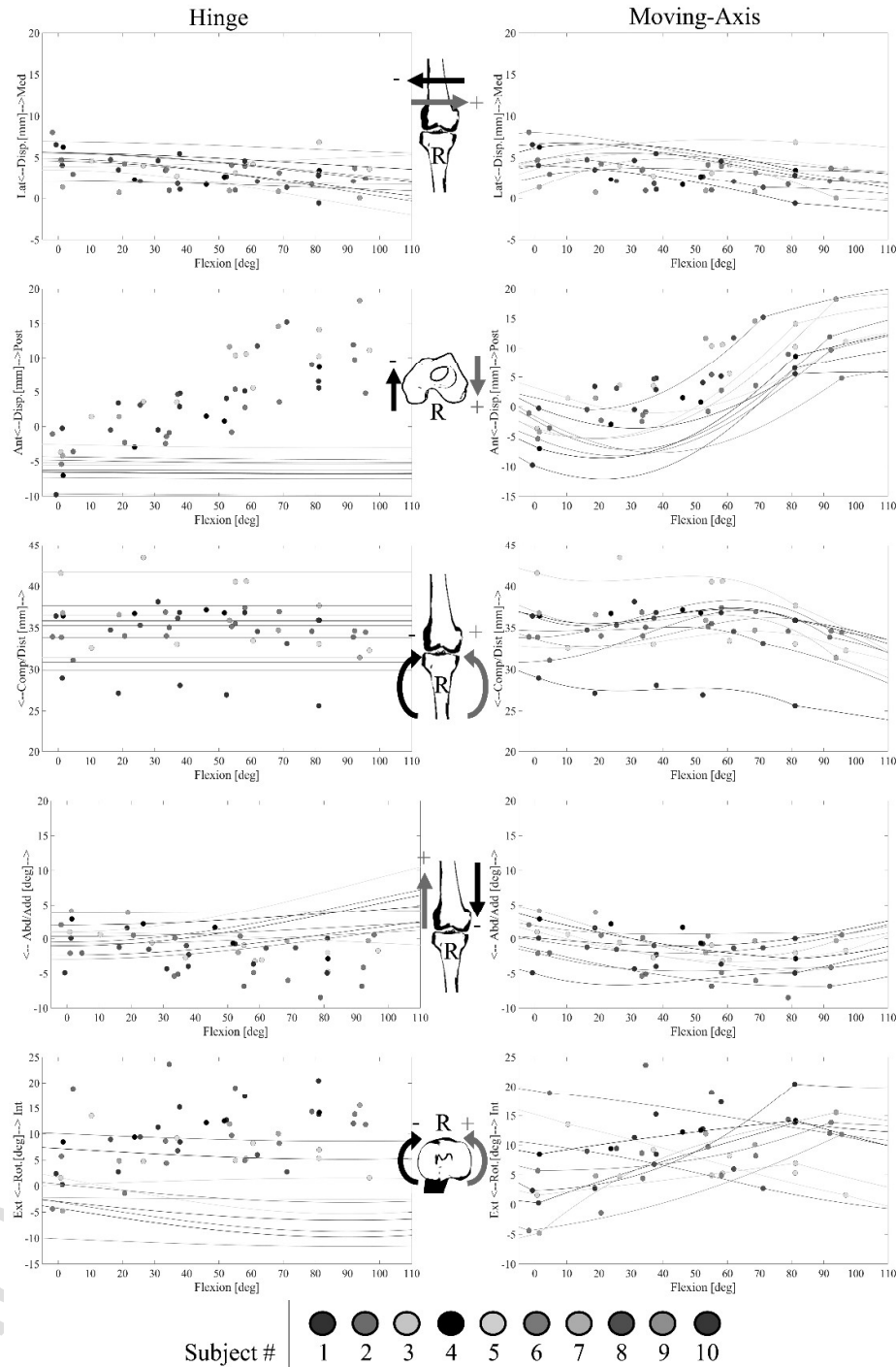


FIGURE 5—Secondary joint kinematic data for hinge and moving-axis models (lines) compared to experimental EOS data (circles) for each subject ($n = 10$). Clinical translations (ML: medial/lateral displacement, AP: anterior/posterior displacement, and CD: compression/distraction) are measured from femur origin relative to tibia. Rotations are measured in the order FE: flexion/extension, AA: abduction/adduction and IE: internal/external rotation from the femoral to the tibial coordinate system.

TABLE 1— Experimental EOS data: Tibiofemoral secondary joint kinematics (mean \pm standard deviation) at quasi-static lunge angles. Averaged kinematic means with and without moving-axis calibration angles (0 and 90). Range of motion (ROM), minimum, and maximum values (mean \pm SD) during knee flexion of $3.48 \pm 5.62^{\circ}$ to $86.59 \pm 8.54^{\circ}$.

Condition	EOS				
	ML (mm)	AP (mm)	CD (mm)	AA ($^{\circ}$)	IE ($^{\circ}$)
EOS_0	4.80 ± 1.87	-3.39 ± 3.42	34.63 ± 3.48	0.05 ± 2.68	5.06 ± 7.59
EOS_20	2.88 ± 1.35	0.61 ± 2.70	35.62 ± 4.13	-1.14 ± 3.22	8.26 ± 6.64
EOS_45	2.68 ± 1.60	4.81 ± 3.89	35.49 ± 3.26	-2.30 ± 2.50	9.61 ± 4.88
EOS_60	2.90 ± 1.19	6.88 ± 5.06	35.01 ± 3.51	-2.59 ± 2.81	10.16 ± 4.08
EOS_90	2.58 ± 2.10	10.58 ± 4.41	33.48 ± 3.32	-2.62 ± 2.49	11.29 ± 5.86
Average (0-90)	3.17 ± 1.62	3.90 ± 3.90	34.84 ± 3.54	-1.72 ± 2.74	8.87 ± 5.81
Average (20-60)	2.82 ± 1.38	4.10 ± 3.88	35.37 ± 3.63	-2.01 ± 2.84	9.34 ± 5.20
min	1.77 ± 1.33	-3.51 ± 3.35	33.07 ± 3.35	-3.57 ± 2.50	2.48 ± 5.15
max	5.02 ± 1.98	10.58 ± 4.41	36.21 ± 3.66	0.35 ± 2.47	14.31 ± 4.84
ROM	3.25 ± 1.48	14.09 ± 5.09	3.14 ± 1.69	3.92 ± 2.11	11.84 ± 5.23

TABLE 2—Moving-axis model output: Tibiofemoral secondary joint kinematics (mean \pm standard deviation) at quasi-static lunge angles. Averaged kinematic means with and without moving-axis calibration angles (0 and 90). Range of motion (ROM), minimum, and maximum values (mean \pm SD) during knee flexion of 3.48 ± 5.62^0 to 86.59 ± 8.54^0 .

Condition	Moving-Axis				
	ML (mm)	AP (mm)	CD (mm)	AA (0)	IE (0)
EOS_0	4.80 ± 1.87	-3.39 ± 3.42	34.64 ± 3.48	0.05 ± 2.68	5.06 ± 7.59
EOS_20	5.30 ± 1.35	-5.58 ± 3.52	34.63 ± 3.30	-1.89 ± 2.71	6.32 ± 5.33
EOS_45	4.99 ± 1.42	-2.98 ± 4.16	35.60 ± 3.52	-2.96 ± 2.29	7.66 ± 4.27
EOS_60	4.11 ± 1.70	1.35 ± 5.63	35.75 ± 3.44	-2.94 ± 2.25	8.36 ± 4.12
EOS_90	2.58 ± 2.10	10.57 ± 4.41	33.48 ± 3.32	-2.62 ± 2.49	11.29 ± 5.86
Average (0-90)	4.35 ± 1.69	-0.00 ± 4.23	34.82 ± 3.41	-2.07 ± 2.48	7.74 ± 5.43
Average (20-60)	4.80 ± 1.49	-2.40 ± 4.44	35.33 ± 3.42	-2.60 ± 2.42	7.45 ± 4.57
min	2.35 ± 1.67	-5.95 ± 3.58	32.83 ± 3.24	-3.41 ± 2.37	2.56 ± 5.20
max	5.72 ± 1.42	10.59 ± 4.41	36.32 ± 3.21	0.06 ± 2.68	13.79 ± 4.04
ROM	3.37 ± 1.39	16.55 ± 4.25	3.48 ± 1.48	3.47 ± 2.19	11.23 ± 5.56

TABLE 3—Hinge model output: Tibiofemoral secondary joint kinematics (mean \pm standard deviation) at quasi-static lunge angles. Averaged kinematic means with and without moving-axis calibration angles (0 and 90). Range of motion (ROM), minimum, and maximum values (mean \pm SD) during knee flexion of $3.48 \pm 5.62^{\circ}$ to $86.59 \pm 8.54^{\circ}$. Hinge knee model has fixed CD of 34.72 ± 3.54 mm.

Condition	Hinge			
	ML (mm)	AP (mm)	AA ($^{\circ}$)	IE ($^{\circ}$)
EOS_0	4.60 ± 1.66	-5.91 ± 1.86	-0.26 ± 2.17	-0.91 ± 5.84
EOS_20	4.08 ± 1.59	-5.96 ± 1.86	0.53 ± 1.93	-1.66 ± 5.94
EOS_45	3.67 ± 1.71	-6.00 ± 1.85	1.15 ± 2.11	-2.24 ± 6.08
EOS_60	3.23 ± 1.88	-6.05 ± 1.83	1.81 ± 2.35	-2.87 ± 6.38
EOS_90	2.75 ± 1.95	-6.10 ± 1.83	2.52 ± 2.55	-3.58 ± 6.72
Average (0-90)	3.67 ± 1.76	-6.00 ± 1.84	1.15 ± 2.22	-2.25 ± 6.19
Average (20-60)	3.66 ± 1.73	-6.00 ± 1.84	1.16 ± 2.13	-2.25 ± 6.13
min	2.54 ± 1.91	-6.08 ± 1.83	-0.01 ± 2.00	-3.34 ± 6.49
max	4.52 ± 1.60	-5.88 ± 1.87	2.90 ± 2.54	-0.49 ± 5.85
ROM	1.98 ± 1.29	0.20 ± 0.12	2.91 ± 2.18	2.85 ± 1.84

TABLE 4—Mean differences \pm standard error between experimental data (EOS) and moving-axis model, EOS and hinge model, and moving-axis and hinge models for quasi-static lunge conditions. Average (\pm SD) are calculated for each clinical measure. *denotes that the clinical measure was statistically significantly different for the given lunge condition.

	Translations (mm)			Rotations ($^{\circ}$)	
	ML	AP	CD	AA	IE
EOS - Moving-Axis Model					
20 Flexion	-2.43 \pm 0.35*	6.19 \pm 0.73*	0.96 \pm 0.32	0.75 \pm 0.40	1.94 \pm 0.88
45 Flexion	-2.31 \pm 0.44*	7.79 \pm 1.02*	-0.11 \pm 0.26	0.66 \pm 0.48	1.95 \pm 1.10
60 Flexion	-1.21 \pm 0.43	5.53 \pm 0.86*	-0.74 \pm 0.20	0.35 \pm 0.41	1.80 \pm 0.97
Average	-1.98 \pm 0.37	6.50 \pm 0.82	0.05 \pm 0.20	0.59 \pm 0.36	1.90 \pm 0.79
EOS - Hinge Model					
20 Flexion	-1.20 \pm 0.35	6.57 \pm 0.51*	0.90 \pm 0.60	-1.66 \pm 0.84	9.92 \pm 1.40*
45 Flexion	-0.99 \pm 0.61	10.82 \pm 1.09*	0.78 \pm 0.67	-3.46 \pm 0.93	11.84 \pm 1.59*
60 Flexion	-0.32 \pm 0.47	12.93 \pm 1.36*	0.29 \pm 0.68	-4.40 \pm 0.97*	13.03 \pm 2.15*
Average	-0.84 \pm 0.45	10.11 \pm 0.88	0.66 \pm 0.62	-3.17 \pm 0.86	11.60 \pm 1.51
Moving-Axis Model – Hinge Model					
20 Flexion	1.23 \pm 0.37	0.38 \pm 0.83	-0.08 \pm 0.63	-2.41 \pm 0.72	7.98 \pm 1.14*
45 Flexion	1.32 \pm 0.50	3.03 \pm 1.13	0.88 \pm 0.84	-4.11 \pm 0.87*	9.90 \pm 1.09*
60 Flexion	0.88 \pm 0.57	7.40 \pm 1.59*	1.03 \pm 0.78	-4.75 \pm 0.93*	11.23 \pm 1.58*
Average	1.14 \pm 0.47	3.60 \pm 1.06	0.61 \pm 0.74	-3.76 \pm 0.82	9.70 \pm 1.10

5

10

15

20 TABLE 5—Model predictive capabilities: Coefficient of determination (R^2) and adjusted R^2
values calculated from model (hinge and moving-axis) and experimental data (EOS) for
quasi-static 20-60 lunge angles combined.

	Model	Translations (mm)			Rotations ($^{\circ}$)	
		ML	AP	CD	AA	IE
R^2	Moving-Axis	0.31	0.71	0.91	0.79	0.67
	Hinge	0.26	0.21	0.70	0.08	0.27
Adj. R^2	Moving-Axis	0.29	0.70	0.90	0.78	0.65
	Hinge	0.23	0.18	0.68	0.05	0.25

25

30

35

40

SUPPLEMENTARY TABLE—Post hoc pairwise comparisons for 15 one-way repeated measures ANOVAs (five clinical measures at three lunge angle conditions) with Bonferroni adjustments due to multiple comparisons ($\alpha = 0.01$). Results include: mean differences (model I-J), standard error, p-value, and confidence intervals.

Clinical Measure	Lunge Angle	(I) model	(J) model	Mean Difference (I-J)	Std. Error	p- value	Confidence Interval	
							Lower Bound	Upper Bound
Medial-Lateral Displacement (mm)	20	EOS	MA	-2.425	0.352	0.000	-3.817	-1.034
		EOS	Hinge	-1.201	0.354	0.024	-2.600	0.199
		MA	Hinge	1.225	0.369	0.027	-0.236	2.686
	45	EOS	MA	-2.311	0.438	0.002	-4.044	-0.578
		EOS	Hinge	-0.991	0.610	0.416	-3.404	1.421
		MA	Hinge	1.320	0.497	0.079	-0.647	3.286
	60	EOS	MA	-1.206	0.429	0.061	-2.900	0.489
		EOS	Hinge	-0.324	0.472	1.000	-2.190	1.541
		MA	Hinge	0.881	0.570	0.470	-1.373	3.136
Anterior-Posterior Displacement (mm)	20	EOS	MA	6.189	0.729	0.000	3.308	9.071
		EOS	Hinge	6.57	0.508	0.000	4.560	8.580
		MA	Hinge	0.381	0.831	1.000	-2.906	3.668
	45	EOS	MA	7.792	1.016	0.000	3.775	11.809
		EOS	Hinge	10.817	1.085	0.000	6.525	15.108
		MA	Hinge	3.025	1.127	0.075	-1.433	7.482
	60	EOS	MA	5.53	0.855	0.000	2.148	8.912
		EOS	Hinge	12.93	1.362	0.000	7.545	18.314
		MA	Hinge	7.4	1.588	0.004	1.122	13.677
Superior-Inferior Displacement (mm)	20	EOS	MA	0.985	0.317	0.038	-0.268	2.238
		EOS	Hinge	0.903	0.604	0.507	-1.485	3.292
		MA	Hinge	-0.081	0.625	1.000	-2.552	2.389
	45	EOS	MA	-0.105	0.259	1.000	-1.130	0.920
		EOS	Hinge	0.778	0.672	0.831	-1.879	3.434
		MA	Hinge	0.883	0.843	0.967	-2.450	4.216
	60	EOS	MA	-0.738	0.203	0.016	-1.539	0.064
		EOS	Hinge	0.293	0.678	1.000	-2.389	2.975
		MA	Hinge	1.031	0.777	0.652	-2.041	4.103
Abduction- Adduction Rotation ($^{\circ}$)	20	EOS	MA	0.750	0.396	0.273	-0.817	2.317
		EOS	Hinge	-1.664	0.841	0.238	-4.991	1.663
		MA	Hinge	-2.414	0.719	0.025	-5.256	0.428
	45	EOS	MA	0.656	0.475	0.601	-1.222	2.534
		EOS	Hinge	-3.455	0.925	0.014	-7.112	0.201
		MA	Hinge	-4.111	0.870	0.003	-7.550	-0.673
	60	EOS	MA	0.349	0.406	1.000	-1.256	1.954
		EOS	Hinge	-4.4	0.968	0.004	-8.227	-0.573
		MA	Hinge	-4.749	0.934	0.002	-8.441	-1.056
Internal-External Rotation ($^{\circ}$)	20	EOS	MA	1.939	0.879	0.164	-1.536	5.415
		EOS	Hinge	9.916	1.403	0.000	4.368	15.463
		MA	Hinge	7.976	1.137	0.000	3.480	12.472
	45	EOS	MA	1.945	1.097	0.330	-2.392	6.283

60	EOS	Hinge	11.841	1.590	0.000	5.554	18.129
	MA	Hinge	9.896	1.086	0.000	5.603	14.189
	EOS	MA	1.801	0.971	0.290	-2.038	5.639
	EOS	Hinge	13.029	2.154	0.001	4.511	21.546
	MA	Hinge	11.228	1.576	0.000	4.998	17.458

ACCEPTED MANUSCRIPT